Polish Geological Institute Special Papers, 7 (2002): 263–270
Proceedings of the IV European Coal Conference

# THREE DIMENSIONAL COAL CHARACTERISATION (MACERAL, MINERAL AND CLEATS) BY MEANS OF X-RAY MICROFOCUS COMPUTER TOMOGRAPHY (μCT)

M. Van GEET[1], P. DAVID[2], R. SWENNEN[1]

A b s t r a c t . One of the aims in coal quality studies, coal bed methane extraction studies, and research on environmental impact of coal, is a full 3D-quantitative characterisation of coal maceral content and distribution, mineral content and cleat system distribution. X-ray microfocus computer tomography, which is a non-destructive technique enabling virtual slicing opaque objects, is an excellent tool. Stacking several slices enables 3D visualisation of the object. The final images show differences in linear attenuation coefficient of X-rays. This linear attenuation coefficient depends on the density and the atomic number of the object. Consequently, components that differ in these parameters can be distinguished. A calibrated dual energy technique allows to extract quantitative information on density and atomic number of the constituents and thus enable maceral and mineral characterisation. The optimal resolution of this technique is 10 μm in three dimensions, which is far better than for classical medical CT (500 × 500 × 1000 μm) used in earlier studies. For this purpose, a correlation between microfocus computer tomography data with data of colour image analysis of reflected light microscopy and with back-scattered electron microscopy data allows maceral and mineral characterisation in three dimensions. Moreover, a calibration with an artificial object with several fracture apertures enables the quantification of cleat sizes.

K e y w o r d s : coal, three dimensions, maceral, mineral content, cleat system, computer tomography.

## INTRODUCTION

Computerised tomography (CT), originally developed in the field of medical sciences, allows 2D or 3D reconstructions of internal features of an object. Because its widespread use and application, geologists have implemented this technique in their studies (Wellington, Vinegar, 1987; Fabre *et al*., 1989; Raynaud *et al*., 1989; Swennen *et al*., 1990; Orsi *et al*., 1994; Boespflug *et al*., 1995; Verhelst *et al*., 1996). These studies clearly demonstrated the power of CT with respect to classical petrography in geological research. However, a disadvantage of classical medical CT is that resolution is moderate (lowest order of magnitude: 60 μm × 60 μm × 1 mm) and too low for detailed geological or material research. Recent developments in the field of microfocus computer tomography (μCT), however, overcome much of this problem. These instruments are based on the same physical principles as medical CT scanners, but obtain much better resolution, which presently is as high as 10 μm × 10 μm × 10 μm.

This contribution introduces the technique and discusses the usefulness of μCT for detailed maceral/mineral and cleat characterisation in coal layers. Adequate techniques will be discussed to document that μCT should not only be used for qualitative visualisation of internal rock features but also for quantitative data acquisition in 3D.

[1] Fysico-chemische Geologie, K.U.Leuven, Celestijnenlaan 200C, B-3001 Heverlee, Belgium
[2] NITG-TNO, Budapestlaan 4, P.O. Box 80015, NL-3508 Utrecht, The Netherlands

## THEORY OF (MICROFOCUS) COMPUTER TOMOGRAPHY

X-ray computerised tomography is a non-destructive medical imaging technique that aims to reconstruct a slice through an object based on the attenuation of X-rays. In principle, for monochromatic X-ray sources the relationship in intensity between incident and attenuated X-rays (respectively $I_0$ and $I$) and $h$, the thickness of the object, may be expressed by Beer's law:

$$\frac{I}{I_0} = \exp(-\mu h) \qquad \text{[Eq. 1]}$$

where μ is the linear attenuation coefficient. At energy levels below 200 kV, linear attenuation is known to depend predominantly on two processes, namely photoelectric absorption and Compton scatter. This may be expressed as (Curry *et al*., 1990):

$$\mu = \rho\left(a + b\frac{Z^{3.8}}{E^{3.2}}\right) \qquad \text{[Eq. 2]}$$

Compton scatter Photoelectric absorption

where ρ is the bulk density of the material, $Z$ is the bulk atomic number of the material, $E$ is the X-ray energy and $a$ and $b$ are energy dependent coefficients. Because of the factor $Z^{3.8}$ in equation 2, it can be concluded that with an increasing atomic number the attenuation will be dominated by photoelectric absorption (Boespflug *et al*., 1994). In classical X-ray radiography (projection according to source-object-detector path) the different internal features of an object become superimposed on the final image. This means that the detected value of one ray is the sum of the attenuation coefficients of every point lying along the X-ray path. To avoid this superpositioning, which masks many features, and to improve resolution, computerised tomography was developed. Here radiographic projections of an object are taken at many angles. In medical sciences this is done by turning the X-ray source and the detector around the object (which in this case is normally a patient). Once these projections are available, a reconstruction algorithm calculates the X-ray attenuation at points (i.e. volume elements or voxels) within the slice. In practice, a filtered back projection is used to reconstruct the tomography slices. The used filter can be changed which leads to noise suppression and loss of optimal resolution or to optimal resolution with lower signal to noise ratio. Stacking several slices of a scanned object permits a three dimensional reconstruction of the object. With classical medical CT, slice by slice is irradiated. The present-day minimum slice thickness is in the order of 1 mm. To achieve 3D images, sequential scans or spiral scans of the patient are made.

The basic physical principles used in μCT are the same as for the medical CT. However, some technical adaptations enable enhanced resolution (Sasov, 1987; Ferreira de Paiva, 1995). The most important one concerns reduction of the spot size of the X-ray source. Reducing the spot size reduces the blurring on the X-ray image (Van Geet *et al*., 2000). It also allows moving the object towards the X-ray source. This will generate a primary magnification of the object, that also results in resolution enhancement. A further point of difference between medical and microfocus computer tomography is that the point source creates a cone beam of X-rays. This enables to scan a part or the whole object at one time. However, an adapted fan beam reconstruction algorithm has to be used for data treatment. However, none of the systems (CT or μCT) are free of artefacts.

The most annoying artefact is *beam hardening*. The reconstruction algorithm in CT and μCT instruments is based on Beer's law [Eq. 1], which is only valid for monochromatic X-rays. As polychromatic X-rays are used, low X-ray energies are preferentially absorbed and thus the X-ray energy spectrum changes while travelling through the object. Backprojections from several projection angles, creates an image where the outer sample border seems to be most attenuated with respect to X-rays. Consequently, the outer border of any object seems to be denser than the inner part. In Figure 1 this artefact is exemplified for a homogeneous aluminium sample. One of the ways to minimise the artefact is placing filters in front of the X-ray source (Joseph, 1981; Jennings, 1988; Van Geet *et al*., 2000). The latter absorbs the light X-ray energies before they reach the object. As shown in Figure 1, filtering techniques can minimise to a large degree the beam hardening. Obviously, for denser materials, the use of thicker filters is needed, which will affect contrast.

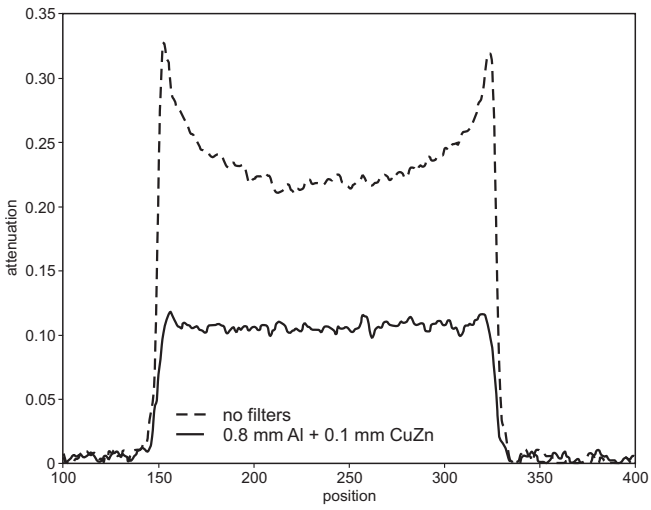


**Fig. 1. Profiles through an aluminium sample of 4 mm in diameter, illustrating the beam hardening effect and the minimisation of this artefact by using metal foils**

Values between lines within image presentations are proportional to X-ray attenuation. It depends mainly on density, effective atomic number of the object and the used X-ray energy [Eq. 2]. It follows that the images are not true visualisations of density differences, nor of differences in effective atomic number within the object. This explains the moderate correlation coefficient between density and attenuation (Van Geet *et al*., 2000).

Scanning homogeneous calibration materials (such as polymers and monominerals) at two energies enables reconstruction of two new images (Alvarez, Macovski, 1976; Kalender *et al*., 1987a, b; Coenen, Maas, 1994; Van Geet *et al*., 2000). This dual energy method, however, requires images free of artefacts, especially free of beam hardening. As stated before, hardware filtering techniques can help, especially if geological samples with unknown materials are studied.

Rearranging Equation 2 results in:

$$\frac{\mu(E)}{\rho} = a(E) + b(E)Z^{3.8} \qquad \text{[Eq. 3]}$$

where coefficients $a$ and $b$ are energy dependent (Dyson, 1973).

The coefficients $a$ an $b$ can be measured by scanning homogeneous reference materials with different known densities and effective atomic numbers. By plotting the mass absorption coefficient of those reference materials versus $Z^{3.8}$ for a standard sample size, it is possible to obtain the coefficients $a$ and $b$ using a linear regression. Once calibrated, the following equations (adapted from Coenen and Maas, 1994) allow to calculate:

$$\rho = \frac{b_h\mu_l - b_l\mu_h}{b_h a_l - b_l a_h} \qquad \text{[Eq. 4]}$$

$$Z = \sqrt[3.8]{\frac{a_l\mu_h - a_h\mu_l}{b_h\mu_l - b_l\mu_h}}$$

where the subscripts $h$ and $l$ refer to values derived from the high and the low energy scan, respectively (in our study $h$ = 130 kV and $l$ = 100 kV). Consequently, it is possible to extract the density (ρ) and the effective atomic number ($Z$), without a priori knowledge of the object.

## COAL MACERAL CHARACTERISATION

### Methodology

The investigated coal is a sample of seam 20 of borehole KS54 (depth 1108.54–1108.68 m) from the Campine Basin, NE Belgium. The seam is identified as Westphalian A and B (Dusar en Goossens, 1991) and classified as high volatile A bituminous coal with a vitrinite reflectance of 0.97% $R_r$. The well was drilled in the framework of a pilot project for research on the possibilities of coal bed methane extraction in the Campine Basin.

From the original impregnated sample with one polished surface, a subsample of 8 mm in diameter was drilled. On the polished surface two traces, perpendicular to the compositional layering, were analysed by colour image analysis (CIA) over a length of approximately 7 mm. Each trace was composed of about 38 images of 768 × 576 pixels, each pixel about 0.35 µm large. The instrument used in this study was a SIS PRO Colour Image Analysis System equipped with a Sony DXC-930 RGB video camera, an Acerview76e monitor (1024 × 1024 pixels) and a Zeiss Axioplan microscope containing an Epi-Plan 50× oil immersion objective and an eyepiece magnification of ×10. This signal of the scanned image is transmitted to the hardware of the SIS PRO using a PC-Pentium II computer and can then be used for different image operations.

In this study, the technique of CIA uses RGB intensity values or HSI (hue, saturation, intensity) information to distinguish between objects of different colour. The different constituents of coal can be differentiated by means of thresholding (David, Fermont, 1993), i.e. defining the upper and lower levels of the colour parameters of each group. This technique enabled the distinction between the three main groups of macerals, i.e. vitrinite, liptinite and inertinite. Moreover, pyrite and binder can be distinguished as well. Unfortunately, the colour characteristics of pyrite and inertinite are very similar. This can induce an error. Furthermore, the instrument is not equipped with a motorised stage. Therefore, the transport of the sample has been performed manually, which undoubtedly introduces additional errors.

Just beneath the polished surface a rock slice was scanned by µCT. The instrument used is a Skyscan 1072 X-ray microfocus computer tomograph. The sample was scanned at two energies, namely 130 and 100 kV, both at 300 µA. For both energies, a beam-hardening filter of 0.8 mm of aluminium and 0.1 mm of a CuZn alloy were used in order to eliminate artefacts.

Therefore, it can be assumed that X-ray energy is not changing while travelling through the coal sample. The basic assumption in this study is that for a given X-ray energy the linear attenuation coefficient linearly depends on density only. This is only valid if the mean atomic number of the three coal components is similar, which is the case. Consequently, a correlation between linear attenuation coefficient and colour image analysis can be worked out. Our approach has, in comparison with the study of Simons *et al*. (1997), apart of the better resolution, the major advantage that beam hardening is eliminated. The latter authors considered this artefact the most important cause of error. The used dual-energy technique furthermore enables to extract physical densities of all distinguishable constituents which is much easier to interpret than linear attenuation.

The reconstruction used was a filtered back projection, which resulted in images of 512 × 512 pixels, each pixel about 21.7 µm large.

In order to investigate the mineral matter (e.g. clay, quartz) present in the coal sample, the polished section was coated with carbon and one trace was studied by back-scattered electron microscopy (BSE). The instrument used is a JEOL-JSM 6400 scanning electron microscope. Operating conditions were 15 kV, 60 µA and about 600 Å beam width. The resulting images were digitally stored as 618 × 618 pixels, each pixel about 0.12 µm large. Again, a non-motorised stage was used which will introduce errors. This technique of BSE enables distinction of components of different atomic number but additional chemical analysis allowed mineralogical identification. The latter was carried out using an exL-LINK energy dispersive X-ray analytical system (EDX) on the scanning electron microscope. The difference in mean atomic number of the several coal macerals is, however, too small to allow differentiation between them. The only components that can be differentiated are clay minerals and pyrite from coal macerals.

### Cross-correlation µCT–CIA–BSE

Figure 2 shows the used µCT slice through the coal sample, scanned at 130 kV together with the position of the trace analysed with CIA and BSE. The compositional layering can be clearly distinguished. In the CIA analysis, not all pixels can be classified as one of the sample constituents. For optimal data

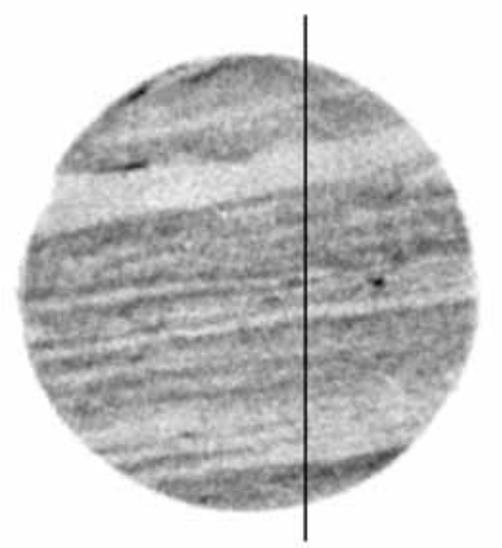

**Fig. 2. µCT reconstruction of one slice through a coal sample of 8 mm in diameter. The maceral layering within the sample is clearly visualised. High attenuating materials correspond with darker colours. The position of the trace along which the correlation between µCT, CIA and BSE was performed, is indicated with a black line**

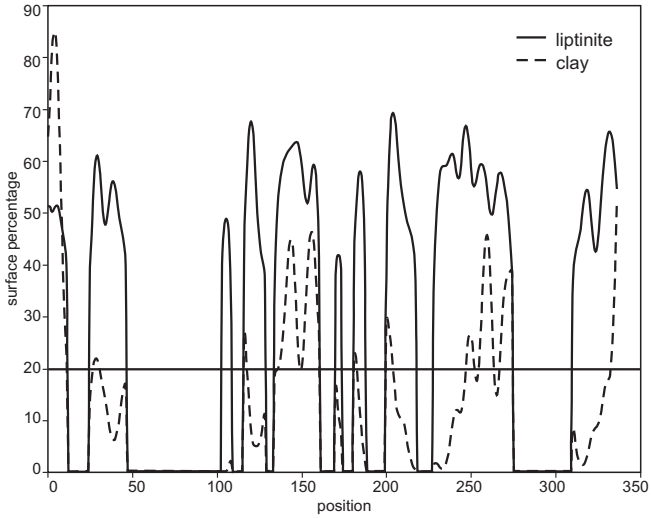


**Fig. 3. Liptinite surface percentages (measured with CIA) and the amount of clay (measured with BSE) along the trace illustrated in figure 2. Where the amount of liptinite is less than its mean value, the signals of liptinite and clay amounts are set to zero. The horizontal line gives the mean value of clay in the remaining datapoints**

treatment, the whole signal is normalised. To be able to perform a multiple linear regression, the data are also smoothed (Simons *et al*., 1997) by FFT-filtering the frequency content with a cut-off frequency of 185 µm.

The positioning of the µCT with respect to the CIA data, was achieved by maximising in the cross-correlation between the surface percentage of the linear attenuation coefficient and vitrinite. Vitrinite was chosen here since it is the most abundant coal component. Therefore, the largest variation in linear attenuation is likely related to this component.

Subsequently, a multiple linear regression is performed with these data. The trace consists of 336 datapoints (samples). The formula (at 130 kV) is:

$$\text{linear attenuation coefficient} = (0.02928 \pm 0.000471) + (0.01949 \pm 0.003141) \times (\text{LIP}) + (0.050769 \pm 0.010319) \times (\text{INE}) + (0.050914 \pm 0.046923) \times (\text{PYR}) - (0.003566 \pm 0.003542) \times (\text{BIN}) \quad \text{[Eq. 5]}$$

where LIP, INE, PYR and BIN denote the surface percentages divided by 100 of liptinite, inertinite, pyrite and binder, respectively. The uncertainties quoted are standard errors of the regression coefficients. The coefficient of multiple determination ($R^2$) between the µCT signal and the predicted signal on all samples is 0.52.

BSE is an outstanding technique in characterising mineral matter in coal. Moreover, the EDX equipment allowed quantifying the amount and the distribution of clay minerals. Where the liptinite signal is above its mean value, the liptinite signal and the clay signal are given in Figure 3. It can be seen that high amounts of clay often (but not always) relates to the occurrence of liptinite. Unfortunately, it is not possible to incorporate the BSE--signal into the CIA-signal, since the clay matter is incorporated in one of the CIA classifications. Consequently, only a semi-quantitative approach can be used. From this dataset, the mean surface percentage of clay within pixels with high liptinite content (pixels with more than the mean liptinite content) is about 20%.

## Density calculation of constituents

The dual-energy technique enables to quantify physical density. This technique is quite sensitive to noise. Therefore, the mean value of ten succeeding slices (about 215 µm in total thickness) was calculated. This procedure seems justified since from a 3D reconstruction of the whole sample it was concluded that the compositional layering was continuous in the third dimension. The results, together with values given in literature, are shown in Table 1.

For vitrinite and binder, the calculated values are very close to the values reported in literature. The calculated density of pyrite deviates somewhat from literature data. The value for inertinite, however, is quite different. These latter constituents occur only very locally and are statistically not really relevant for the multiple linear regression analysis. Consequently, it can be accepted that their calculated densities are statistically less reliable. Moreover, CIA-differentiation between pyrite and inertinite is not obvious. This might partially explain the overestimated calculated density of inertinite.

**Table 1**

**Comparison of the density measurements in this study and density found in literature**

| Component | Density found in literature [g/cm$^3$] | Calculated density [g/cm$^3$] |
|---|---|---|
| Vitrinite | 1.3 | 1.31 |
| Liptinite | >1.3 | 1.74 |
| Inertinite | 1.6 | 5.64 |
| Pyrite | 5.0 | 4.66 |
| Binder | 1.2 | 1.21 |

The calculated density of liptinite is also overestimated. Liptinite, however, is a major component, which easily can be differentiated with CIA. But as shown liptinite often occurs in close interrelation with clay minerals. If a mean density of clay of 3 g/cm$^3$ is assumed, the recalculated density of liptinite lowers to values reported in literature.

### 3D coal characterisation

The performed cross-correlation provides now the basic data to visualise and quantify coal macerals within three dimensions in the sample. The regression constants can be used as threshold values for coal components, like vitrinite for example. Within the studied sample, a volume of about 7% of voxels containing 100% vitrinite could be calculated. Voxels containing 90% vitrinite together with 10% of another constituent, make up about 23% of the sample volume. The distribution of these voxels is visualised in Figure 4. The vitrinite layering clearly appears in three dimensions.

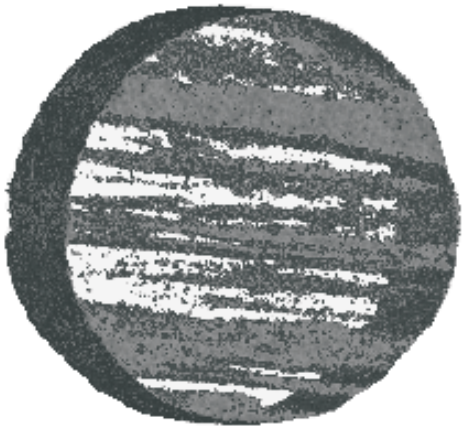

**Fig. 4. The 3D distribution of vitrinite within the studied coal sample. The outer surface has been highlighted as well**

## COAL FRACTURE (CLEAT) ANALYSIS

### Calibration

Objects of 8 mm in diameter were scanned by µCT, resulting in a voxelsize of 21.7 µm in three dimensions. For calibration a plexiglass cylinder was cut in two halves and each halve was polished to avoid roughness. A special specimen holder was developed, which kept one halve of the cilinder fixed and allowed to move the other halve by means of a micrometerscrew with a stepsize of 20 µm. The calibration was performed on artificial fractures with aperures between 20 and 200 µm at a 20 micron stepsize and with apertures between 200 and 400 µm with a 40 µm stepsize. Two possible techniques in measuring the fracture apertures were tested (Fig. 5). The first technique, called the full width at half maximum measurement (FWHM), measures the thickness at the attenuation value, taken halfway between the mean attenuation of plexiglass and the minimum attenuation value within the fracture. The second technique integrates the amount of lost attenuation over the entire fracture profile (Johns *et al*., 1993; Keller, 1998). In practice, the fracture profile is subtracted from the minimum attenuation value of plexiglass and the remaining peak is summed. For the calibration, an averaging over 100 sequential profiles was carried out as to minimise the influence of noise. The result of both measuring techniques is shown on Figure 6. From the correlation between real fracture aperture and FWHM or integration values, it can be concluded that a very significant correlation can be worked out. However, notice that for the FWHM technique a deviation from a linear trend occurrs for small fracture apertures. This deviation is reduced by adapting the digital filter used in the filtered backprojection algorithm. Changing this filter, however, results in sharper boundaries, but more noise. The result of using an adapted filter is also plotted in Figure 6. Altough a better correlation is achieved now, the integration technique provides more accurate results and thus is preferred.

Subsequently, the calibration is validated by measuring fractures of two halve cylinders of plexiglass and glass, which are kept at specified distances by means of metal foils of 100, 200, 300 and 400 microns. For the plexiglass testobject, the results can be easily plotted on the same axes as used before. The results of the glass object need to be normalised as the attenuation value of plexiglass and glass is different. Moreover, as an additional test, the thickness of the foils can be measured seperately, if the attenuation coefficient of the material is

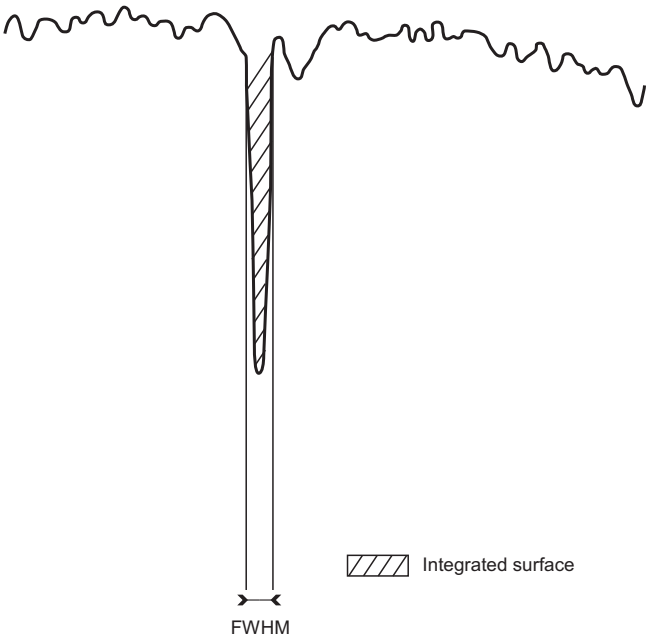


**Fig. 5. Illustration of the possible techniques to measure fracture apertures, i.e. measurement of full width at half maximum (FWHM) of the gap or integration of the missing values over the gap**

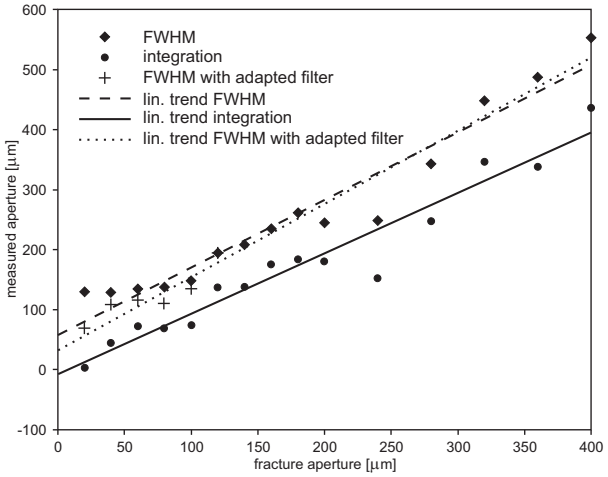


**Fig. 6. Plot of the real fracture apertures versus measured fracture apertures by means of FWHM and integration technique. For the FWHM measurements, a deviation from the linear trend is apparent for small apertures. An adapted reconstruction algorithm enables to optimise the FWHM measurement even for small fracture apertures**

known. These testobjects confirm the linear correlation between fracture aperture and µCT data.

Next, a statistical treatment of the results is performed to be able to ascertain a defined confidence interval. Therefore, one profile through the fracture was measured at several sequential slices. A coefficient of variation of about 8% was deduced. Averaging the values of 5 sequential slices, however, reduces the coefficient of variation to about 5%. The latter results in larger voxels, namely 21.7 by 21.7 by 108.5 microns.

## Application

This 3D-fracture characterisation technique is tested on a coal sample of 8 mm in diameter. Figure 7 shows a 2D slice through a coal sample of the Campine Basin (Belgium). The investigated sample is again a subsample of seam 20 of borehole KS54 from the Campine Basin (Belgium).

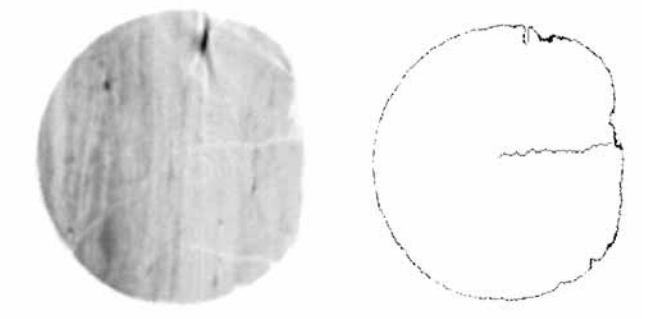

**Fig. 7. µCT reconstruction of one slice through a coal sample of 8 mm in diameter (left). The orientation of the cleats (fractures) is clearly visible. The aperture is measured for the fracture illustrated as a black line in the sample (right). The mean fracture aperture is 52 µm**

µCT-scanning allows to visualise the natural fracture system (cleats) within the sample. The latter are dominantly oriented perpendicular to the layering of the several coal components. For the central fracture, which is shown on the right side of Figure 7, the aperture was measured at every pixel. The mean fracture aperture is 52 µm with a standard deviation of 19 µm.

## CONCLUSION

Microfocus computer tomography allows a thorough and quick three dimensional coal characterisation. In this study, the technique was calibrated for samples of 8 mm in diameter so that a high resolution is achieved, but results can be easily extrapolated to larger samples. Consequently, microfocus computer tomography is able to characterise samples at many sizes and to visualise and quantify features at different resolution levels. This might lead to an integrated approach of a scaling down philosophy, characterising core samples down to very small cylinders.

## REFERENCES

ALVAREZ R.E., MACOVSKI A., 1976 — Energy-selective reconstructions in X-ray computerized tomography. *Phys. Med. Biol.*, **21**: 733–744.

BOESPFLUG X., ROSS N., LONG B., DUMAIS J.F., 1994 — Tomodensitométrie axiale: relation entre l'intensité tomographique et la densité de la matičre. *Can. J. Earth Sci.*, **31**: 426–434.

BOESPFLUG X., LONG B.F.N., OCCHIETTI S., 1995 — Cat-scan in marine stratigraphy: a quantitative approach. *Marine Geology*, **122**: 281–301.

COENEN J.C.G., MAAS J.G., 1994 — Material classification by dual-energy computerized X-ray tomography. International symposium on computerized tomography for industrial applications: 120–127.

CURRY T.S., DOWDEY J.E., MURRY R.C., 1990 — Christensen's Physics of diagnostic radiology. Lea & Febiger, London.

DAVID P., FERMONT W.J.J., 1993 — Application of color image analysis in coal petrology. *Org. Geochem.*, **20**: 747–758.

DUSAR M., GOOSSENS W.R.A., 1991 — Potentieel van steenkoollaag-methaanwinning in het Kempens Bekken. *Energie & Milieu*, **6**: 202–203.

DYSON N.A., 1973 — X-rays in atomic and nuclear physics. Longman Group Limited, London.

FABRE D., MAZEROLLE F., RAYNAUD S., 1989 — Caractérisation tomodensitométrique de la porosité et de la fissuration de roches sédimentaires. In: Rock at great depth (Maury, Fourmaintraux, Eds.): 297–304. Balkema, Rotterdam.

FERREIRA de PAIVA R., 1995 — Développement d'un microtomographe X et application à la charactérisation des roches réservoirs. Thèse de doctorat de l'Université de Paris VI.

JENNINGS F.J., 1988 — A method for comparing beam-hardening filter materials for diagnostic radiology. *Med. Phys*., **15**: 588–599.

JOHNS R.A., STEUDE J.S., CASTANIER L.M., ROBERTS P.V., 1993 — Nondestructive measurements of fracture aperture in crystalline rock cores using X-ray computed tomography. *J. Geoph. Res*., **98**: 1889–1900.

JOSEPH P.M., 1981 — Artifacts in computed tomography. In: Radiology of the skull and brain: technical aspects of computed tomography (T.H. Newton, T.G. Potts, Eds.), vol. 5: 3956–3992. The CV Mosby company, St Louis.

KALENDER W., BAUTZ W., FELSENBERG D., SÜSS C., KLOTZ, E., 1987a — Materialselektive Bildgebung und Dichtemessung mit der Zwei-Spektren-Methode I. Grundlagen und Methodik. *Digit. Bilddiagn*., **7**: 66–72.

KALENDER W., FELSENBERG D., SÜSS C., 1987b — Materialselektive Bildgebung und Dichtemessung mit der Zwei--Spektren-Methode III. Knochenmineralbestimmung mit CT an der Wirbelsäule. *Digit. Bilddiagn*., **7**: 170–176.

KELLER A., 1998 — High resolution, non-destructive measurement and characterization of fracture apertures. *Int. J. Rock Mech. Sci*., **35**: 1037–1050.

ORSI T.H., EDWARDS C.M., ANDERSON A.L., 1994 — X-ray computed tomography: a nondestructive method for quantitative analysis of sediment cores. *J. Sediment. Res*., **A64**: 690–693.

RAYNAUD S., FABRE D., MAZEROLLE F., GERAUD Y., LATIÈRE H.J., 1989 — Analysis of the internal structure of rocks and characterization of mechanical deformation by a non-destructive method : X-ray tomodensitometry. *Tectonophysics*, **159**: 149–159.

SASOV A.Y., 1987 — Microtomography, I. Methods and equipment, II. Examples of applications. *J. Microscopy*, **147**: 169–192.

SIMONS F.J., VERHELST F., SWENNEN R., 1997 — Quantitative characterization of coal by means of microfocal X-ray computed microtomography (CMT) and color image analysis (CIA). *Int. J. Coal Geol*., **34**: 69–88.

SWENNEN R., POOT B., MARCHAL G., 1990 — Computerized tomography as a tool in reservoir characterization. *Zbl. Geol. Paläont*. Teil I: 1105–1124.

Van GEET M., SWENNEN R., WEVERS M., 2000 — Quantitative analysis of reservoir rocks by microfocus X-ray computerised tomography. *Sed. Geol*., **132**: 25–36.

VERHELST F., DAVID P., FERMONT W., JEGERS L., VERVOORT A., 1996 — Correlation of 3D-computerized tomographic scans and 2D-colour image analysis of Westphalian coal by means of multivariate statistics. *Int. J. Coal Geol*., **29**: 1–21.

WELLINGTON S.L., VINEGAR H.J., 1987 — X-ray computerized tomography. *J. Petrol. Tech*.: 885–898.